



Universiteit
Leiden
The Netherlands

CUTE reveals escaping metals in the upper atmosphere of the ultrahot Jupiter WASP-189b

Sreejith, A.G.; France, K.; Fossati, L.; Koskinen, T.T.; Egan, A.; Cauley, P.W.; ... ; De Almeida Vidotto, A.

Citation

Sreejith, A. G., France, K., Fossati, L., Koskinen, T. T., Egan, A., Cauley, P. W., ... De Almeida Vidotto, A. (2023). CUTE reveals escaping metals in the upper atmosphere of the ultrahot Jupiter WASP-189b. *Astrophysical Journal Letters*, 954(1). doi:10.3847/2041-8213/acef1c

Version: Publisher's Version
License: [Creative Commons CC BY 4.0 license](https://creativecommons.org/licenses/by/4.0/)
Downloaded from: <https://hdl.handle.net/1887/3716188>

Note: To cite this publication please use the final published version (if applicable).



CUTE Reveals Escaping Metals in the Upper Atmosphere of the Ultrahot Jupiter WASP-189b

A. G. Sreejith^{1,2} , Kevin France¹ , Luca Fossati² , Tommi T. Koskinen³ , Arika Egan¹ , P. Wilson Cauley¹ , Patricio. E. Cubillos^{2,4} , S. Ambily¹ , Chenliang Huang⁵ , Panayotis Lavvas⁶ , Brian T. Fleming¹ , Jean-Michel Desert⁷ , Nicholas Nell¹ , Pascal Petit⁸ , and Aline Vidotto⁹

¹ Laboratory for Atmospheric and Space Physics, University of Colorado, UCB 600, Boulder, CO 80309, USA; sreejith.aickara@lasp.colorado.edu, sreejith.aickara@oeaw.ac.at

² Space Research Institute, Austrian Academy of Sciences, Schmiedlstrasse 6, A-8042 Graz, Austria

³ Lunar and Planetary Laboratory, University of Arizona, Tucson, AZ 85721-0092, USA

⁴ INAF—Osservatorio Astrofisico di Torino, Via Osservatorio 20, I-10025 Pino Torinese, Italy

⁵ Shanghai Astronomical Observatory, CAS, Shanghai, 200030, People's Republic of China

⁶ Groupe de Spectroscopie Moléculaire et Atmosphérique, Université de Reims, Champagne-Ardenne, CNRS UMR-F-7331, France

⁷ Anton Pannekoek Institute for Astronomy, University of Amsterdam, P.O. Box 94249, Noord Holland, NL-1090 GE Amsterdam, The Netherlands

⁸ Institut de Recherche en Astrophysique et Planétologie, Université de Toulouse, CNRS, CNES, 14 avenue Edouard Belin, F-31400 Toulouse, France

⁹ Leiden Observatory, Leiden University, P.O. Box 9513, 2300 RA, Leiden, The Netherlands

Received 2023 June 20; revised 2023 July 29; accepted 2023 August 10; published 2023 August 31

Abstract

Ultraviolet observations of ultrahot Jupiters, exoplanets with temperatures over 2000 K, provide us with an opportunity to investigate if and how atmospheric escape shapes their upper atmosphere. Near-ultraviolet transit spectroscopy offers a unique tool to study this process owing to the presence of strong metal lines and a bright photospheric continuum as the light source against which the absorbing gas is observed. WASP-189b is one of the hottest planets discovered to date, with a dayside temperature of about 3400 K orbiting a bright A-type star. We present the first near-ultraviolet observations of WASP-189b, acquired with the Colorado Ultraviolet Transit Experiment (CUTE). CUTE is a 6U NASA-funded ultraviolet spectroscopy mission, dedicated to monitoring short-period transiting planets. WASP-189b was one of the CUTE early science targets and was observed during three consecutive transits in 2022 March. We present an analysis of the CUTE observations and results demonstrating near-ultraviolet (2500–3300 Å) broadband transit depth ($1.08_{-0.08}^{+0.08}\%$) of about twice the visual transit depth indicating that the planet has an extended, hot upper atmosphere with a temperature of about 15,000 K and a moderate mass-loss rate of about $4 \times 10^8 \text{ kg s}^{-1}$. We observe absorption by Mg II lines (R_p/R_s of $0.212_{-0.061}^{+0.038}$) beyond the Roche lobe at $>4\sigma$ significance in the transmission spectrum at a resolution of 10 Å, while at lower resolution (100 Å), we observe a quasi-continuous absorption signal consistent with a “forest” of low-ionization metal absorption dominated by Fe II. The results suggest an upper atmospheric temperature ($\sim 15,000$ K), higher than that predicted by current state-of-the-art hydrodynamic models.

Unified Astronomy Thesaurus concepts: Exoplanets (498); Near ultraviolet astronomy (1094); Astronomical techniques (1684); Spectroscopy (1558); Exoplanet atmospheres (487); Transits (1711); Exoplanet atmospheric composition (2021); Space observatories (1543)

Supporting material: machine-readable tables

1. Introduction

WASP-189b is an ultrahot Jupiter (UJ) orbiting a bright ($V = 6.64$ mag) A4 star with a period of about 2.7 days (Anderson et al. 2018; Lendl et al. 2020). UJs are planets with equilibrium temperatures (T_{eq}) higher than 2000 K and for which the continuum absorption level in the optical and near-infrared is mainly controlled by H^- opacity (e.g., Arcangeli et al. 2018; Parmentier et al. 2018; Fossati et al. 2021). The high T_{eq} , and thus large pressure scale height, of these planets favor atmospheric characterization observations both in transmission and emission. In the case of WASP-189b, Lendl et al. (2020) collected high-precision optical primary transit and secondary eclipse photometry with the CHaracterising ExO-Planets Satellite (CHEOPS) satellite (Benz et al. 2021) and inferred that the dayside planetary atmosphere is rather

unreflective (low albedo; Lendl et al. 2020) at a temperature of about 3400 K, when assuming inefficient heat redistribution. Recently, Prinoth et al. (2022) collected and analyzed High Accuracy Radial Velocity Planet Searcher (HARPS) high-resolution optical spectra of WASP-189b during the primary transit, which led them to detect absorption by TiO and several metals such as Fe, Ti, Cr, Mg, V, and Mn. Their analysis found absorption depths attributed to neutral atoms, consistent with local thermodynamic equilibrium (LTE) based on hydrostatic and chemical equilibrium models. They also noted a deviation of their model from observations for strong metal ions and suggested non-LTE effects, hydrodynamic escape, or nightside condensation as possible causes.

UJs are typically found orbiting bright intermediate-mass stars (Casasayas-Barris et al. 2019), with a large range of high-energy (X-ray and extreme ultraviolet, EUV; together XUV) luminosity ranging from a few times solar (later than spectral type A3/A4) to orders of magnitude subsolar (earlier than spectral type A3/A4; Fossati et al. 2018). The high atmospheric temperatures of UJs and the fact that they typically



Original content from this work may be used under the terms of the [Creative Commons Attribution 4.0 licence](https://creativecommons.org/licenses/by/4.0/). Any further distribution of this work must maintain attribution to the author(s) and the title of the work, journal citation and DOI.

orbit early-type stars (F and A types) that can have very strong (later than spectral type A4) or very weak (earlier than spectral type A4) XUV emission make these planets ideal laboratories for studying the physics of planetary upper atmospheres and, in particular, the separate roles of XUV and UV irradiation in heating the atmosphere and driving escape (Fossati et al. 2018).

Atmospheric escape from exoplanets can be observed with excited metal, He, and H lines (typically H Ly α , H Balmer lines, and He I(2^3S) triplet at $\approx 10,830$ Å in addition to neutral and ionized metals). Ultraviolet (UV) wavelengths probe many of these lines (see, e.g., Fossati et al. 2015).¹⁰ UV transmission spectroscopy observations are typically conducted at far-UV (FUV) wavelengths (e.g., Ly α), but in the near-UV (NUV) band stars have a significantly stronger and more uniform emission than in the FUV (Haswell et al. 2012; Llama & Shkolnik 2015). Furthermore, the NUV range contains strong lines of several abundant metals, such as Mg and Fe, that effectively probe upper atmospheres and escape (Fossati et al. 2010; Haswell et al. 2012; Sing et al. 2019; Cubillos et al. 2020, 2023), as well as molecular bands probing atmospheric haze and cloud condensations (Lothringer et al. 2022).

We present the analysis and results obtained from three NUV transit observations of WASP-189b collected with the Colorado Ultraviolet Transit Experiment (CUTE) mission, which is a NASA 6U CubeSat (with stowed dimensions of $11.0 \times 23.7 \times 36.2$ cm) CubeSat carrying on board a rectangular Cassegrain telescope feeding light into a low-resolution NUV (2479–3306 Å) spectrograph (Fleming et al. 2018; Egan et al. 2023; France et al. 2023). CUTE monitors transiting exoplanets orbiting bright stars to study the upper atmospheres and star–planet interaction processes. The early spectral type and brightness of the host star make the WASP-189 system ideal for CUTE observations (Sreejith et al. 2019).

This Letter is organized as follows. We describe the observations in Section 2 and the data analysis in Section 3. We discuss the results and their implications in Section 4. Finally, in Section 5 we summarize our findings and future work based on CUTE data.

2. Observations

We observed WASP-189b for three transits with CUTE on 2022 March 23, 2022 March 26, and 2022 March 28 (visits 1, 2, and 3, respectively). Each transit (one CUTE visit) was observed over a period approximately 5 times the transit duration covering the planet’s orbital phase from -0.2 to 0.2 . A typical CUTE orbit is 96 minutes, and we observed the target for 16 orbits in visits 2 and 3, while in visit 1 the target has been observed for just 13 orbits due to observational constraints and a spacecraft reset (France et al. 2023). The number of exposures per satellite orbit varies from one to five, depending on target position and pointing constraints that include the Sun angle, the Moon angle, the elevation cutoff with Earth’s limb, the spacecraft settling time, and the location of the satellite with respect to the South Atlantic Anomaly (SAA) and polar keepout zones (Suresh et al. 2023). These constraints, combined with the spacecraft settling time of up to 15 minutes and data processing time of 70 s per exposure, limit the total number of exposures per eclipse to

five. Each 300 s CUTE exposure consists of a two-dimensional spectrogram of 2048×100 pixels centered around the spectrum covering the 2480–3306 Å spectral range with a spectral resolving power of about 1000 with a signal-to-noise ratio of about 25 per resolution element for a 300 s exposure. The CCD is passively cooled and maintains the temperature between -10°C and -5°C with occasional spikes in temperature during ground station passes and pointing anomalies. CUTE, with its single star tracker, provides pointing jitter (standard deviation) of better than $6''$ for about 60% of the observations (Egan et al. 2023), but some observations after the orbital dayside and close to the SAA are known to have higher jitter, leading to lower resolution and noisier spectra. We refer readers to Egan et al. (2023) for a detailed discussion on CUTE’s on-orbit performance. The data were reduced following the methods described by Sreejith et al. (2022) to obtain wavelength and flux-calibrated one-dimensional spectra.

3. Data Analysis

Our data analysis scheme follows a similar methodology as described by Cubillos et al. (2020, 2023). For each visit, we first construct “white” light curves by integrating the flux in each exposure over the wavelength range to increase our signal-to-noise ratio (Kreidberg et al. 2014). This white-light curve is used to characterize the instrumental systematics. Then, we divide the systematics model from the raw data and combine the systematics-corrected data from all visits into spectral light curves at a range of spectral binnings, and we extract the transmission spectra of the target as explained in detail in Section 3.1.

We carry out an initial data quality screening on our observations to remove outliers. We select all observations where the R.A. and decl. jitter values are below $6''$ and the CCD temperature is below -5°C . This cutoff is to enable uniformity in all the data points, as observations with larger jitter will have lower fluxes due to part of the spectrum falling outside our extraction region, and possibly vignetting of the telescope beam by the edges of the slit (Sreejith et al. 2022). These selection criteria are applied to both visits 2 and 3. In the case of visit 1 due to a spacecraft reset, R.A. and decl. jitter information was not available, and we incorporated a flux cutoff to reject bad jitter observations, based on the findings from visits 2 and 3. We also noticed that observations after an orbital day (Sun-lit side) lead to low fluxes from visits 1 and 2 (in visit 3 these observations were also flagged as bad jitter) possibly due to scatter effects as in these latitudes we observe through a much larger column of the Earth’s atmosphere.

3.1. Individual Visits

We identify systematics using a visit-specific white-light analysis, integrating the entire spectrum to create each individual data point. This assumes that the instrumental systematics behave similarly over the integrated range (Kreidberg et al. 2014). We fit the raw light curves ($F_\lambda(t)$) with a parametric transit and systematics models similar to Cubillos et al. (2023) as a function of time (t), CUTE orbital phase (ϕ), and jitter vector (j_i):

$$F_\lambda(t) = T_\lambda(t) S_\lambda(t, \phi, j_i), \quad (1)$$

¹⁰ The metastable He I(2^3S) triplet at ≈ 10830 Å can probe upper atmospheres in alternative to the ultraviolet (UV) band, but the spectral energy distribution (SED) of intermediate-mass stars inhibits the formation of He I(2^3S) (Oklopčić & Hirata 2018; Oklopčić 2019).

Table 1
Jitter Parameters

Jitter Parameters	
CCD temperature (TMP)	Median of CCD temperature during a 300 s exposure.
R.A. jitter (RAJ)	Standard deviation of R.A. during a 300 s exposure.
Decl. jitter (DCJ)	Standard deviation of decl. during a 300 s exposure.
Roll jitter (ROJ)	Standard deviation of Roll during a 300 s exposure.
Geolatitude (GLA)	Latitude of the satellite during a 300 s exposure.
Geolongitude (GLO)	Longitude of the satellite during a 300 s exposure.
Geoaltitude (GAL)	Altitude of the satellite during a 300 s exposure.
Sun angle (SAN)	Angle between the telescope boresight and the Sun

where $T_\lambda(t)$ is a Mandel & Agol (2002) transit model and $S_\lambda(t, \phi, j_i)$ is a model of the CUTE instrumental systematics similar to the scheme used in Cubillos et al. (2023). We obtain the best-fitting parameters and uncertainties from a Levenberg–Marquardt optimization and a Markov Chain Monte Carlo (MCMC) sampling, respectively, employing the open-source MC3 package¹¹ (Cubillos et al. 2017), which implements the Snooker Differential-evolution MCMC algorithm of ter Braak & Vrugt (2008). This enables us to arrive at statistically robust parameter estimations.

Our transit model fits the input data using the planet orbital parameters, planet–star radius ratios $R_p/R_s(\lambda)$, out-of-transit stellar fluxes $F_s(\lambda)$, and limb-darkening coefficients. We used the planet orbital parameters computed by Lendl et al. (2020) using CHEOPS observations. These parameters, except for midtransit time, $R_p/R_s(\lambda)$, and $F_s(\lambda)$, were kept fixed during the fitting and MCMC process. The midtransit time is fitted by applying a Gaussian prior according to the measured value from Lendl et al. (2020). Uncertainties are propagated according to the epoch of the CUTE observations. The limb-darkening parameters were computed based on the stellar properties using the open-source code of Espinoza & Jordán (2015). This enables us to compute the limb-darkening coefficients over our wavelength range based on the PHOENIX stellar model (Husser et al. 2013) according to WASP-189 stellar properties from Lendl et al. (2020).

The effects of systematics on transit measurements are well documented in the literature (e.g., Brown et al. 2001; Wakeford et al. 2016; Sing et al. 2019; Cubillos et al. 2020, 2023). Similar to the systematics accounted for in Hubble Space Telescope (HST)/STIS observations, we use a time-dependent polynomial that can account for stellar activity and another polynomial that can account for orbit-dependent systematics. Building on the work of Sing et al. (2019) and Cubillos et al. (2023), we also make use of jitter data to decorrelate the instrumental systematics from the transit signal. The jitter parameters we use are summarized in Table 1. Employing these three sets of information we have a polynomial systematic model that is up to cubic in time, quartic in telescope phase, and linear in one of the jitter parameters as follows:

$$\begin{aligned}
S_\lambda(t, \phi, j_i) = & 1 + a_0(t - t_0) + a_1(t - t_0)^2 + a_2(t - t_0)^3 \\
& + b_0(\phi - \phi_0) + b_1(\phi - \phi_0)^2 \\
& + b_2(\phi - \phi_0)^3 + b_3(\phi - \phi_0)^4 \\
& + c_0(j_i - \langle j_i \rangle),
\end{aligned}
\tag{2}$$

Table 2
BIC/AICc Best-fit Models

Systematics Model (t -deg, ϕ -deg, jitter)	BIC	AICc	χ^2_{red}	R_p/R_s	Phase Offset
Visit 1 (3, 2, GAL)	46.54	46.47	1.01	$0.101^{+0.009}_{-0.016}$	$0.0148^{+0.003}_{-0.005}$
Visit 2 (1, 4, GLA)	113.83	108.19	3.4319	$0.107^{+0.006}_{-0.020}$	$0.0162^{+0.0492}_{-0.0057}$
Visit 3 (1, 2, GLA)	71.10	65.11	1.7933	$0.108^{+0.010}_{-0.014}$	$-0.0016^{+0.0073}_{-0.0028}$

Note. The polynomial degree and jitter parameter of the systematics model are shown in the first column.

where a_k , b_k , and c_k are the polynomial coefficients of the fit and t_0 and ϕ_0 are the reference values for the time and phase, set as midtransit time $t_0 = T_0$ and the CUTE telescope midphase $\phi_0 = 0.2$, respectively. $\langle j_i \rangle$ denotes the mean value of the jitter parameter j_i along the visit as summarized in Table 1.

We make use of both the Bayesian model selection approach (see, e.g., Trotta 2007) and Akaike information criterion corrected for small sample sizes (AICc; Liddle 2007) for model selection. All combinations of polynomials and jitter parameters from Equation (2) are compared for this approach. Both approaches in the case of our analysis prefer models that minimize both the Bayesian information criterion (BIC) and AIC values. We refer the reader to Cubillos et al. (2023) for an additional general discussion of the BIC and AIC comparison used in our analysis methods.

Table 2 summarizes the best-fitting models for each visit. We see visit-specific and CUTE orbit-specific systematics in our data. Our analysis indicates stronger systematics in visit 2 compared to the other two visits. This is evident by the larger BIC, AIC, and reduced χ^2 values. We found that the fits were optimized with a phase offset between the UV and optical light curves of about ~ 0.015 , although it is unclear if this is a physical effect or an artifact of the CUTE data collection systematics. Our analysis gives self-consistent transit depths for all visits as shown in Figure 1 with best-fit polynomials in time and telescope phase within the range found for light curve detrending in HST/STIS analysis (Cubillos et al. 2023; Gressier et al. 2023).

3.1.1. Divide-white Spectral Extraction

The CUTE transmission spectra are obtained by the “divide-white” spectral analysis method of Kreidberg et al. (2014),

¹¹ <https://mc3.readthedocs.io/>

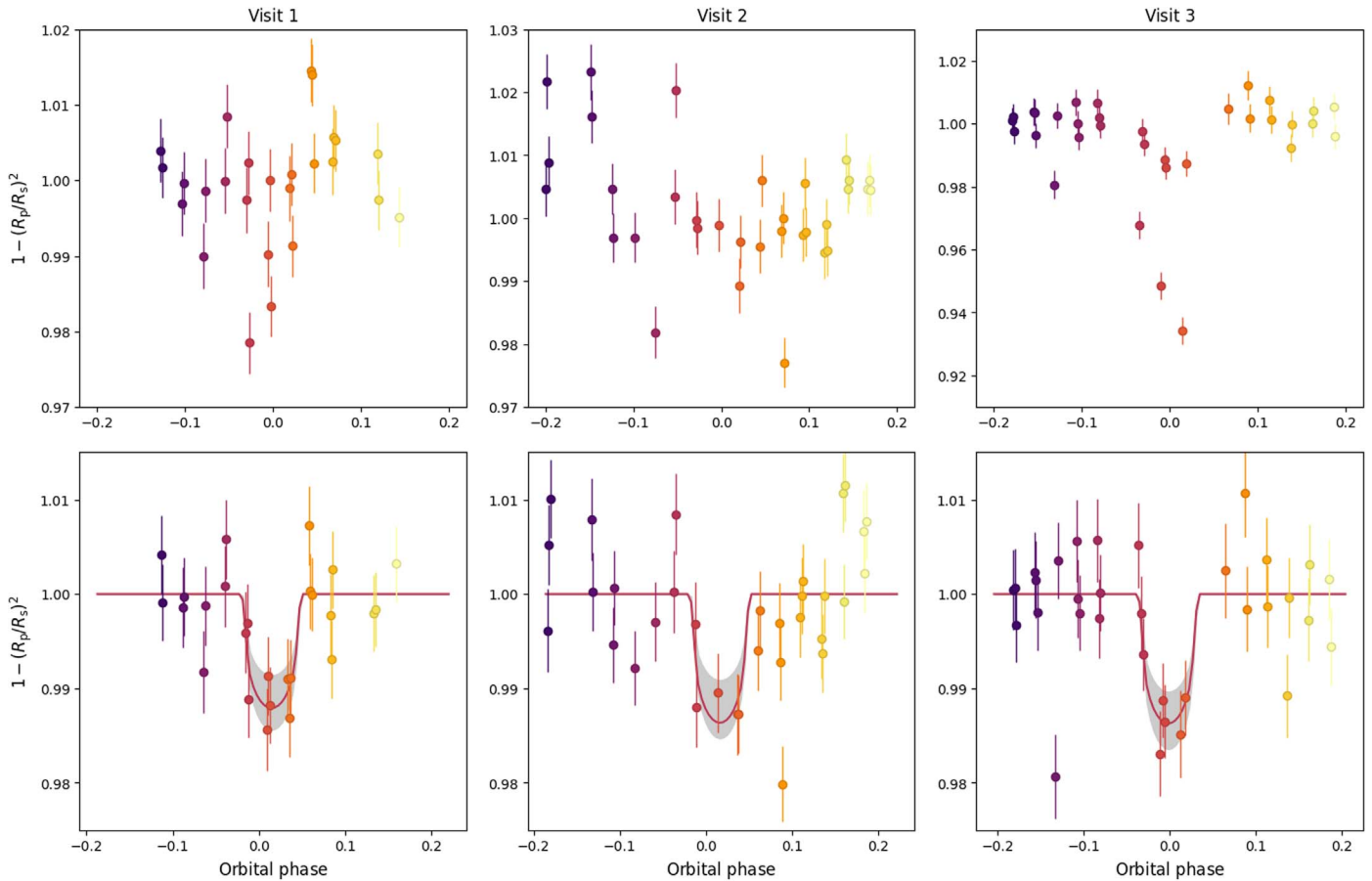


Figure 1. NUV white-light curve fitting of WASP-189b. The top panels show the raw light curve. The bottom panels show the systematics-corrected light curves following the best BIC/best AICc. The solid orange lines denote the transit model of the best fit. The data points are colored based on the CUTE satellite orbits (from purple to yellow in increasing order).

described in detail for NUV transit spectroscopy in Cubillos et al. (2020). We create visit-specific nonparametric instrumental systematics by dividing the white-light curves by the best-fit transit model (see Section 3.1). This is based on the assumption that the instrumental systematics have a weak wavelength dependence, guided by our analysis of raw light curves. These systematics are divided out of the raw spectral light curve and the resultant light curve is dominated by the transit signal where instrument systematics have been mitigated.

We estimate uncertainties of the best-fit white-light transit model from the standard deviation of the distribution for the white-light transit model, generated from the white-analysis posterior distribution. Then we use the error-propagation formula (Bevington & Robinson 2003) to account for all uncertainties throughout the steps involved to construct the nonparametric systematics model and obtain the systematics-corrected light curve.

This systematics-corrected data are divided into wavelength bins of our choice and coadded to create wavelength-specific data points. These data are fitted with a Mandel & Agol (2002) transit model with a fixed orbital period (P), inclination (i), and semimajor axis to stellar radius ratio (a/R_s) parameters, and a Gaussian prior for the midtransit epoch based on our results from the white-light fit. The limb-darkening coefficients are also calculated at each wavelength bin from the stellar model as described in Section 3.1 and are kept fixed during the fit. Hence, the free parameters for these fits are the midtransit time,

the transit depth, and the out-of-transit flux in each wavelength bin. Since the light curve combines data from different epochs, we fit the out-of-transit flux level of each visit as an individual free parameter.

4. Results and Discussion

Figure 2 (top) shows the combined transit light curve in an 800 Å bin centered at 2900 Å (full CUTE band). This light curve is generated using the divide-white method described in the previous section and points toward a transit depth of $1.08^{+0.08}_{-0.08}\%$, larger than the optical transit depth (0.496%; Lendl et al. 2020) of WASP-189b and consistent with the previous HST observations of UHJs (Sing et al. 2019; Cubillos et al. 2020; Lothringer et al. 2022). Broadband NUV transits with this depth suggest we are probing the upper atmosphere of this planet that is unaffected by clouds and hazes and hence the broadband transit we observe would most likely be due to a combination of metal lines in the upper atmosphere of the planet. To understand the origin of this excess absorption we create a transmission spectrum at finer wavelength bins as shown in Figure 2. The $R_p/R_s(\lambda)$ ratio increases as we move toward shorter wavelengths as observed for WASP-121b and WASP-178b (Sing et al. 2019; Lothringer et al. 2022). This indicates stronger NUV absorption by WASP-189b at the shortest NUV wavelengths sampled by CUTE (2500–2800 Å), with an NUV planet radius (R_p/R_s) of about $0.127^{+0.012}_{-0.010}$. Figure 2 (middle) displays the transmission spectrum in

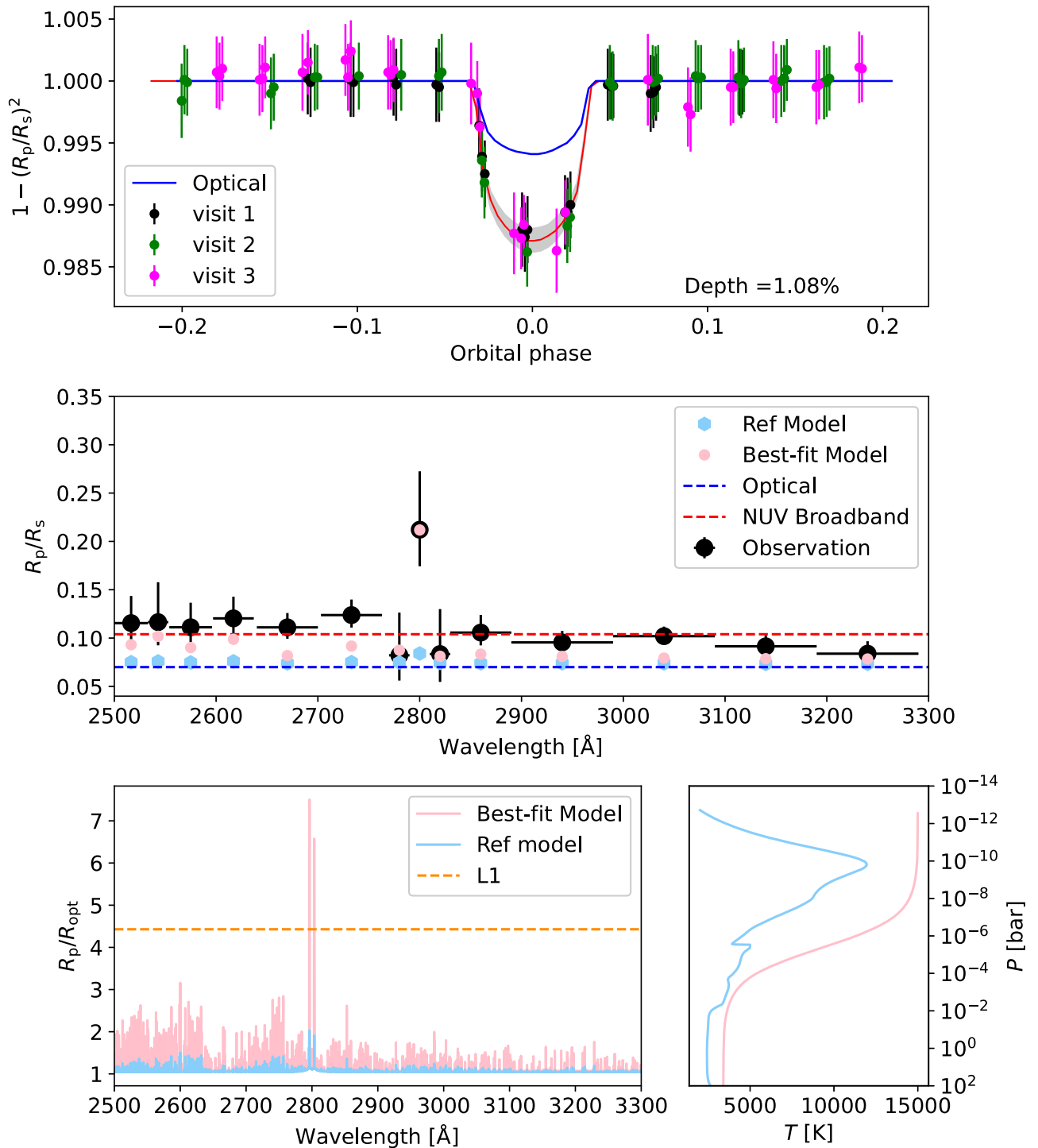


Figure 2. NUV broadband light curve and transmission spectrum obtained from WASP-189b analysis. Top: broadband NUV light curve of WASP-189b for a 800 Å bin centered at 2900 Å. Middle: transmission spectrum at variable resolutions (black filled circles) with reference and best-fit models (light blue and pink, respectively). Bottom left: high-resolution models showing the variation of the ratio of planetary radius (R_p) with optical planetary radius (R_{opt}) as a function of wavelength. Bottom right: T - P profiles used to generate the transmission spectrum (reference model in light blue and the best-fit model in pink).

different wavelength bins. This transmission spectrum indicates significant evidence of planetary absorption of the Mg II h and k lines (2802.705 and 2795.528 Å). The absorption peak at 2800 Å is consistent with a model spectrum with strong Mg II h and k lines, as shown in Figure 2 (bottom left) and discussed below. The 10 Å bin centered at 2800 Å has a planetary radius ratio (R_p/R_s) of $0.212^{+0.038}_{-0.061}$, which is significantly higher than the broadband NUV radius ratio of 0.105. This is ≈ 3 times the

optical radius of the planet at a significance of $\sim 4.15\sigma$. This analysis indicates there are Mg II ions beyond the L1 Lagrange point for this planet and hence they are escaping. We provide our quantitative analysis of the mass-loss rate in the following section.

To constrain the extent of the atmosphere of WASP-189b based on the observed NUV transit depths, we first construct a physical model of the whole atmosphere to predict density

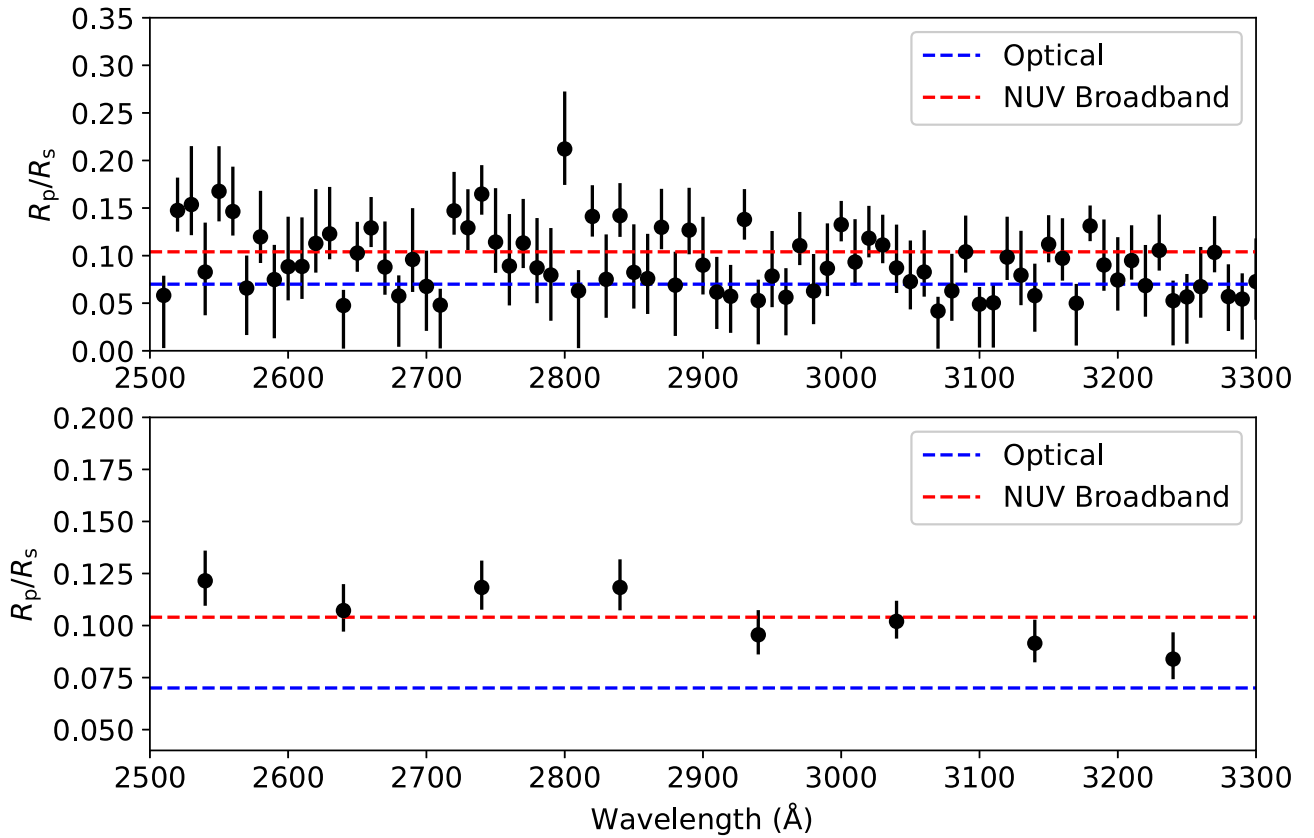


Figure 3. Top: transmission spectrum at 10 Å bin. Bottom: transmission spectrum at 100 Å bin.

profiles of the possible absorbers (hereafter, the reference model). We model the lower and middle atmosphere with the photochemical–thermal structure model of Lavvas & Arfaux (2021), assuming global redistribution of heat and constituents. At pressures lower than $1 \mu\text{bar}$, we use the multispecies hydrodynamic escape model of Koskinen et al. (2022), updated to include the elements H, He, Mg, Si, Fe, O, C, N, Na, K, S, Ca, and relevant ions (Huang et al. 2023). For the stellar spectrum, ranging from the FUV to the infrared, we use the spectral energy distribution (SED) computed with the PHOENIX stellar atmosphere code (Husser et al. 2013) based on the stellar parameters from Lendl et al. (2020). In the X-ray and EUV range, we follow the results of Fossati et al. (2018) and multiply the solar emission spectrum from Claire et al. (2012) by a factor of 3.

Figure 2 (bottom right) shows the temperature–pressure (T – P) profile predicted by our reference model. The discontinuity at the lower boundary of the escape model indicates that the radiative transfer schemes of the two models are not yet perfectly self-consistent, but the results are close enough for illustration purposes. A more refined coupling will be pursued in future work. Figure 2 (middle) also compares the transit depths based on the reference model with the observations, showing that the model falls well short of the observations. Two main reasons contribute to this discrepancy. First, the radiative cooling rates in the thermosphere due to H and metal line emissions are relatively high and offset much of the stellar XUV heating that would otherwise power escape. This lowers the temperature in the upper atmosphere and reduces the mass-loss rate. Second, the predicted absorption in the NUV is mostly due to Fe and Mg ions and second ionization of these

elements by stellar XUV radiation is significant, reducing the density of the first ionization states.

To arrive at our best-fit model, we follow a simpler, more empirical approach. Effectively, we fix the T – P profile in the model until the predicted upper atmospheric opacities match the observations. The best-fit temperature profile is also shown in Figure 2. We increase the temperature in the lower and middle atmosphere to the dayside temperature of 3400 K (Lendl et al. 2020). We now model the composition in the lower and middle atmosphere by using the chemical equilibrium model GGChem (Woitke et al. 2018). This is acceptable because the temperature in the middle atmosphere is so high that Fe and Mg are strongly ionized thermally. In the upper atmosphere, we disable the energy equation solver and run the escape model with a fixed temperature profile. This allows us to still include photoionization of the metal ions at high altitudes. Our best-fit model is designed to match the Mg II transit depth, as illustrated in Figure 2 (bottom left). Intriguingly, the shape of the model transit depths is also close to the observations outside of the Mg II doublet, particularly on the blue side, indicating additional opacity from Fe II absorption lines.

The best-fit model implies a mass-loss rate of about $4 \times 10^8 \text{ kg s}^{-1}$, which is more than 300 times higher than the mass-loss rate predicted by our reference model. This new mass-loss rate, however, is still consistent with stellar XUV energy-limited mass-loss rate (e.g., Erkaev et al. 2007) with a heating efficiency of about 10% in the upper atmosphere (assuming that escape is powered by stellar radiation at 0.1–100 nm, which is conservative in this case). The best-fit temperature profile is also significantly hotter than the reference model temperature profile in the upper atmosphere. This could

be explained either by an additional source of direct heating or lower radiative cooling rates. The difference between the observed transit depths that coincide with the Fe II lines and the best-fit model could arise from uncertainties in photoionization and recombination rates. A higher fraction of Fe II over Fe III could produce a larger transit depth that is still consistent with solar abundances.

5. Summary and Conclusions

We present the first near-ultraviolet transit observations of WASP-189 from the CUTE CubeSat. This is one of the hottest planets that has so far been observed in the NUV. Our findings of excess NUV absorption in the planet are consistent with previous HST transit observations of similar exoplanets (Fossati et al. 2010; Sing et al. 2019). We find a dramatic increase in absorption below 3000 Å, with transit depths decreasing toward the optical value at $\lambda > 3100$ Å. The Mg II h and k lines are observed at a depth of about 3 times the visible planetary transit depth in a 10 Å bin centered on the Mg II h and k lines at 2800 Å. Our modeling indicates the presence of Mg II and possibly Fe II ions in the upper atmosphere. A fit to the Mg II transit depth indicates that Mg ions are escaping the atmosphere. Based on our best-fit model to these observations that constrain the extent and temperature of the upper atmosphere, the total mass-loss rate of all species is $4 \times 10^8 \text{ kg s}^{-1}$. We attempted to reproduce the observed transmission spectrum with a state-of-the-art hydrodynamic upper atmosphere model accounting for the most relevant known atmospheric processes, but this led to an underestimate of the transit depths. Therefore, we increased the upper atmospheric temperature to fit the observed strength of the Mg II h and k absorption. We found that the observations can be fitted with a temperature of about 15,000 K in the upper atmosphere, which is about 5000 K higher than the peak temperature predicted by the self-consistent model.

There are just a few exoplanets with published NUV observations, and most have been spectroscopic observations obtained by HST (Fossati et al. 2010; Haswell et al. 2012; Sing et al. 2019; Wakeford et al. 2020; Lothringer et al. 2022; Cubillos et al. 2023; Gressier et al. 2023) and a few are photometric with multiple instruments (Folsom et al. 2018; Salz et al. 2019; Corrales et al. 2021). Despite the differences between the systems observed in the NUV, an extended upper atmosphere seems to be a common feature. Some of the UHJs previously observed in the NUV orbit rather faint stars (e.g., WASP-12b, WASP-121b). Therefore, the host star brightness makes WASP-189b a key target for future multiwavelength observations aimed at deepening our understanding of these ultrahot worlds.

Acknowledgments

CUTE is supported by NASA grants NNX17AI84G and 80NSSC21K1667 (PI: K. France) to the University of Colorado Boulder. This project was funded in part by the Austrian Science Fund (FWF) J4595-N and J4596-N. L.F. acknowledges financial support from the Austrian Forschungsförderungsgesellschaft FFG project CARNIVALS P885348. A.V. acknowledges funding from the European Research Council (ERC) under the European Union’s Horizon 2020 research and innovation program (grant agreement No. 817540, ASTROFLOW). This research has made use of NASA’s Astrophysics

Data System Bibliographic Services. We thank the anonymous referee for their comments that helped to improve the paper.

Software: MC3 (Cubillos et al. 2017), NUMPY (Harris et al. 2020), SCIPY (Virtanen et al. 2020), MATPLOTLIB (Hunter 2007), IPYTHON (Pérez & Granger 2007), and BIBMANAGER (Cubillos 2019).

Appendix A Stellar and Planetary Parameters

The stellar and planetary parameters used in the fit are as shown in Table 3.

Table 3
WASP-189b Orbital and Stellar Parameters Input to Calculate the Best-fit CUTE Light Curves

Orbital Parameter	
Orbital period (days) P	2.724033
inclination (degrees) i	84.03
semimajor axis to stellar radius ratio (au) a	0.05053
Transit epoch (MJD) T_0	58926.04169599991
Stellar parameters	
Effective temperature (K)	8000
log10(gravity) [cgs units]	3.9
Stellar metallicity [M/H]	0.29
Microturbulent velocity (km s^{-1})	2.7

Appendix B Transmission Spectrum of WASP-189b

Tables 4 and 5 represents truncated transmission spectrum at the 100 Å and 10 Å bins, respectively. The full table is

Table 4
NUV Transmission Spectrum at the 100 Å Bin

λ (Å)	R_p/R_s
2540	$0.121^{+0.015}_{-0.012}$
2640	$0.107^{+0.013}_{-0.010}$
2740	$0.118^{+0.013}_{-0.010}$
2840	$0.118^{+0.014}_{-0.011}$
2940	$0.096^{+0.012}_{-0.009}$
3040	$0.102^{+0.009}_{-0.008}$
3140	$0.091^{+0.011}_{-0.009}$
3240	$0.084^{+0.013}_{-0.009}$

(This table is available in its entirety in machine-readable form.)

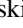

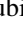

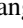
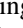
Table 5
NUV Transmission Spectrum at the 10 Å Bin

λ (Å)	R_p/R_s
2510	$0.0582^{+0.0207}_{-0.0554}$
2520	$0.1475^{+0.0345}_{-0.0223}$
2530	$0.1537^{+0.0614}_{-0.0322}$

(This table is available in its entirety in machine-readable form.)

available in machine-readable format. Figure 3 represents the transmission spectrum in these two resolutions.

ORCID iDs

A. G. Sreejith  <https://orcid.org/0000-0002-4166-4263>
 Kevin France  <https://orcid.org/0000-0002-1002-3674>
 Luca Fossati  <https://orcid.org/0000-0003-4426-9530>
 Tommi T. Koskinen  <https://orcid.org/0000-0003-3071-8358>
 Arika Egan  <https://orcid.org/0000-0002-4701-8916>
 P. Wilson Cauley  <https://orcid.org/0000-0001-9207-0564>
 Patricio. E. Cubillos  <https://orcid.org/0000-0002-1347-2600>
 S. Ambily  <https://orcid.org/0000-0002-0506-0825>
 Chenliang Huang  <https://orcid.org/0000-0001-9446-6853>
 Panayotis Lavvas  <https://orcid.org/0000-0002-5360-3660>
 Brian T. Fleming  <https://orcid.org/0000-0002-2129-0292>
 Jean-Michel Desert  <https://orcid.org/0000-0002-0875-8401>
 Nicholas Nell  <https://orcid.org/0000-0001-7131-7978>
 Pascal Petit  <https://orcid.org/0000-0001-7624-9222>
 Aline Vidotto  <https://orcid.org/0000-0001-5371-2675>

References

- Anderson, D. R., Temple, L. Y., Nielsen, L. D., et al. 2018, arXiv:1809.04897
 Arcangeli, J., Désert, J.-M., Line, M. R., et al. 2018, *ApJL*, **855**, L30
 Benz, W., Broeg, C., Fortier, A., et al. 2021, *ExA*, **51**, 109
 Bevington, P. R., & Robinson, D. K. 2003, *Data Reduction and Error Analysis for the Physical Sciences* (Boston, MA: McGraw-Hill)
 Brown, T. M., Charbonneau, D., Gilliland, R. L., Noyes, R. W., & Burrows, A. 2001, *ApJ*, **552**, 699
 Casasayas-Barris, N., Pallé, E., Yan, F., et al. 2019, *A&A*, **628**, A9
 Claire, M. W., Sheets, J., Cohen, M., et al. 2012, *ApJ*, **757**, 95
 Corrales, L., Ravi, S., King, G. W., et al. 2021, *AJ*, **162**, 287
 Cubillos, P., Harrington, J., Lored, T. J., et al. 2017, *AJ*, **153**, 3
 Cubillos, P. E. 2019, *bibmanager: A BibTeX Manager for LaTeX Projects*, v1.1.0, Zenodo, doi:10.5281/zenodo.2547042
 Cubillos, P. E., Fossati, L., Koskinen, T., et al. 2020, *AJ*, **159**, 111
 Cubillos, P. E., Fossati, L., Koskinen, T., et al. 2023, *A&A*, **671**, A170
 Egan, A., Nell, N., Suresh, A., et al. 2023, *AJ*, **165**, 64
 Erkaev, N. V., Kulikov, Y. N., Lammer, H., et al. 2007, *A&A*, **472**, 329
 Espinoza, N., & Jordán, A. 2015, *MNRAS*, **450**, 1879
 Fleming, B. T., France, K., Nell, N., et al. 2018, *JATIS*, **4**, 014004
 Folsom, C. P., Fossati, L., Wood, B. E., et al. 2018, *MNRAS*, **481**, 5286
 Fossati, L., Haswell, C. A., Froning, C. S., et al. 2010, *ApJL*, **714**, L222
 Fossati, L., Haswell, C. A., Linsky, J. L., & Kislyakova, K. G. 2015, in *Characterizing Stellar and Exoplanetary Environments*, Astrophysics and Space Science Library, Vol. 411, ed. H. Lammer & M. Khodachenko (Cham: Springer), 59
 Fossati, L., Koskinen, T., Lothringer, J. D., et al. 2018, *ApJL*, **868**, L30
 Fossati, L., Young, M. E., Shulyak, D., et al. 2021, *A&A*, **653**, A52
 France, K., Fleming, B., Egan, A., et al. 2023, *AJ*, **165**, 63
 Gressier, A., Lecavelier des Etangs, A., Sing, D. K., et al. 2023, *A&A*, **672**, A34
 Harris, C. R., Millman, K. J., van der Walt, S. J., et al. 2020, *Natur*, **585**, 357
 Haswell, C. A., Fossati, L., Ayres, T., et al. 2012, *ApJ*, **760**, 79
 Huang, C., Koskinen, T., Lavvas, P., & Fossati, L. 2023, *ApJ*, **951**, 123
 Hunter, J. D. 2007, *CSE*, **9**, 90
 Husser, T. O., Wende-von Berg, S., Dreizler, S., et al. 2013, *A&A*, **553**, A6
 Koskinen, T. T., Lavvas, P., Huang, C., et al. 2022, *ApJ*, **929**, 52
 Kreidberg, L., Bean, J. L., Désert, J.-M., et al. 2014, *Natur*, **505**, 69
 Lavvas, P., & Arfaux, A. 2021, *MNRAS*, **502**, 5643
 Lendl, M., Csizmadia, S., Deline, A., et al. 2020, *A&A*, **643**, A94
 Liddle, A. R. 2007, *MNRAS*, **377**, L74
 Llama, J., & Shkolnik, E. L. 2015, *ApJ*, **802**, 41
 Lothringer, J. D., Sing, D. K., Rustamkulov, Z., et al. 2022, *Natur*, **604**, 49
 Mandel, K., & Agol, E. 2002, *ApJL*, **580**, L171
 Oklopčić, A. 2019, *ApJ*, **881**, 133
 Oklopčić, A., & Hirata, C. M. 2018, *ApJL*, **855**, L11
 Parmentier, V., Line, M. R., Bean, J. L., et al. 2018, *A&A*, **617**, A110
 Pérez, F., & Granger, B. E. 2007, *CSE*, **9**, 21
 Prinoth, B., Hoeijmakers, H. J., Kitzmann, D., et al. 2022, *NatAs*, **6**, 449
 Salz, M., Schneider, P. C., Fossati, L., et al. 2019, *A&A*, **623**, A57
 Sing, D. K., Lavvas, P., Ballester, G. E., et al. 2019, *AJ*, **158**, 91
 Sreejith, A. G., Fossati, L., Ambily, S., et al. 2022, *PASP*, **134**, 114506
 Sreejith, A. G., Fossati, L., Fleming, B. T., et al. 2019, *JATIS*, **5**, 018004
 Suresh, A., France, K., Nell, N., et al. 2023, *JATIS*, submitted
 ter Braak, C. J. F., & Vrugt, J. A. 2008, *Stat. Comput.*, **18**, 435
 Trotta, R. 2007, *MNRAS*, **378**, 72
 Virtanen, P., Gommers, R., Oliphant, T. E., et al. 2020, *NatMe*, **17**, 261
 Wakeford, H. R., Sing, D. K., Evans, T., Deming, D., & Mandell, A. 2016, *ApJ*, **819**, 10
 Wakeford, H. R., Sing, D. K., Stevenson, K. B., et al. 2020, *AJ*, **159**, 204
 Voitke, P., Helling, C., Hunter, G. H., et al. 2018, *A&A*, **614**, A1